



# A Confined Two-peaked Solar Flare Observed by EAST and SDO

Liang Zhang<sup>1,2</sup>, Ruisheng Zheng<sup>1,2,3,8</sup>, Zhike Xue<sup>2</sup>, Changhui Rao<sup>4,5,6,8</sup>, Qing Lin<sup>7</sup>, Zhimao Du<sup>7,8</sup>, Jiawen Yao<sup>7</sup>, Libo Zhong<sup>4,5</sup>, and Yao Chen<sup>1,3</sup>

<sup>1</sup> Institute of Space Sciences, Shandong University, Weihai 264209, China; [ruishengzheng@sdu.edu.cn](mailto:ruishengzheng@sdu.edu.cn), [duzhm@sstm.org.cn](mailto:duzhm@sstm.org.cn), [chrao@ioe.ac.cn](mailto:chrao@ioe.ac.cn)

<sup>2</sup> Yunnan Key Laboratory of the Solar Physics and Space Science, Kunming 650011, China

<sup>3</sup> Institute of Frontier and Interdisciplinary Science, Shandong University, Qingdao 266237, China

<sup>4</sup> Institute of Optics and Electronics, Chinese Academy of Sciences, Chengdu 610209, China

<sup>5</sup> National Laboratory on Adaptive Optics, Chengdu 610209, China

<sup>6</sup> University of Chinese Academy of Sciences, Beijing 100049, China

<sup>7</sup> Shanghai Astronomy Museum, Shanghai 201306, China

Received 2023 November 2; revised 2023 December 16; accepted 2023 December 20; published 2024 March 20

## Abstract

The solar flare is one of the most violent explosions, and can disturb the near-Earth space weather. Except for commonly single-peaked solar flares in soft X-ray, some special flares show intriguing a two-peak feature that is deserved much more attentions. Here, we reported a confined two-peaked solar flare and analyzed the associated eruptions using high-quality observations from Educational Adaptive-optics Solar Telescope and Solar Dynamics Observatory. Before the flare, a magnetic flux rope (MFR) formed through partially tether-cutting reconnection between two sheared arches. The flare occurred after the MFR eruption that was confined by the overlying strong field. Interestingly, a small underlying filament immediately erupted, which was possibly destabilized by the flare ribbon. The successive eruptions were confirmed by the analysis of the emission measure and the reconnection fluxes. Therefore, we suggest that the two peaks of the confined solar flare are corresponding to two episodes of magnetic reconnection during the successive eruptions of the MFR and the underlying filament.

**Key words:** Sun: activity – Sun: corona – Sun: flares – Sun: magnetic fields – Sun: filaments – prominences

**Online material:** animations

## 1. Introduction

Solar eruptions, including solar flares and coronal mass ejections (CMEs), are violent explosions on the Sun, which can release the high-energy ions and a large amount of magnetized plasma to the interplanetary space and thus significantly influence space weather. It is generally believed that the solar eruptions have fundamental structures, such as magnetic flux ropes (MFRs), filaments, etc. (Liu 2020; Patsourakos et al. 2020). MFRs are groups of coherently twisted magnetic field lines that wrap around a central axis and filaments are cold, and dense plasma suspended in a hot corona (Martin 1998; Mackay et al. 2010). They are twist/sheared magnetic structures that are full of magnetic energy (Forbes 2000; Low 2001). During an eruption, the magnetic energy is converted to heat, bulk kinetic energy and fast particle energy. However, the trigger mechanism and subsequently evolution of the solar eruptions are still not fully understood.

In the studies of past decades, many physical models have been proposed to interpret the trigger mechanism of solar eruptions. The models can be mainly divided into two categories: the magnetic reconnection models, such as the tether-cutting model (Moore et al. 2001), flux-cancellation model (van Ballegooijen & Martens 1989)

and breakout model (Antiochos et al. 1999); the ideal magnetohydrodynamics (MHD) models, for instance, the kink instability model (Török et al. 2004; Fan 2005) and torus instability model (Kliem & Török 2006). After initiation, solar flares are intimately related with CMEs. But not every solar flare can be accompanied by a CME. According to whether they are accompanied by the CMEs or not, solar flares are divided into two categories: eruptive flares and confined flares. The confined flare is often accompanied by failed/confined eruption of filaments or MFRs. In the failed/confined eruptions, the filament/MFRs first experienced a fast acceleration, and then quickly decelerated by some reasons. Eventually, they stop at a height or fall back to the Sun that without the occurrence of CMEs (Ji et al. 2003; Yang et al. 2019).

Among numerous solar flares, most of them show a single-peak at GOES X-ray profiles during their impulsive phase. However, there are some unique flares showing two-peaked feature during impulsive phase. They should attend attention but the observations are still rare. Ning et al. (2018) analyzed a confined M2-class flare with intriguing two-peak observed in hard X-rays. They present obvious two steps of loop-loop interaction induced by the two-peaked flare. In addition, they revealed the first step energy release was mainly for nonthermal particles acceleration, and that the second step energy release was mainly for plasma heating through

<sup>8</sup> Corresponding authors.

analyzing the data from RHESSI and NoRH. Zheng et al. (2023) reported another case with two-peak feature in soft X-ray profile and its derivative. They suggest that the two-peak feature was caused by the eruption and deformation of an MFR. Therefore, the two-peaked flares often contain more physical information and correspond to a more complex evolution process. The study of the two-peaked flare can help us understand the evolution of solar eruptions.

Besides, some observations reported that the solar eruptions can be triggered by moving magnetic features (MMFs) (Sterling et al. 2010; Paraschiv et al. 2020; Joshi et al. 2022). As for MMFs, they are persistent activity around a sunspot (Harvey & Harvey 1973). A sunspot is usually surrounded, or in part, by a zone of stationary magnetic field. This zone is called sunspot's "moat." The MMFs exhibit as small magnetic features which move away from the sunspot to the boundary of the moat region. They usually have a higher velocity than the average moat flow. Actually, the MMFs can be classified into two groups according to whether the emerged polarities are coupled or not. They are further divided into three types. Type I MMFs are small magnetic dipoles. Type II and Type III MMFs are unipolar polarities that are separately the same and opposite with the magnetic polarity of the parent sunspot. After emergence, the MMFs can continuously converge to and cancel with the polarity inversion lines (PILs) and thus trigger solar eruptions with a similar manner of the flux-cancellation model (van Ballegooijen & Martens 1989).

In this article, we report a two-peaked confined flare associated with MMFs. The two-peaked flare was induced by successive eruptions of an MFR and a filament. Two eruptions were both without CMEs.

## 2. Observations and Data Analysis

The confined two-peaked flare occurred at the NOAA active region (AR) 13 076 on 2022 August 12, and was associated with successive eruptions of an MFR and a filament. We mainly use the data from Solar Dynamics Observatory (SDO) (Pesnell et al. 2012) and Educational Adaptive-optics Solar Telescope (EAST) (Rao et al. 2022). The formation and eruption of the MFR were recorded by Atmospheric Imaging Assembly (AIA) (Lemen et al. 2012) onboard SDO. The AIA images have a pixel size of 0''.6 and a cadence of 12 s. The eruption of the filament was captured by the high resolution observations from EAST and CHASE/H $\alpha$  Imaging Spectrograph (HIS) (Li et al. 2022). The EAST was built at Shanghai Astronomy Museum with the pixel resolutions of 0''.12 for H $\alpha$  and TiO. The CHASE/HIS provides H $\alpha$  figures with a pixel spatial resolution of 0''.52. The MMFs and the evolution of the magnetic field in the source region were checked by Helioseismic and Magnetic Imager (HMI; Scherrer et al. 2012) onboard SDO, with the cadence of 45 s and pixel scale of 0''.6.

In addition, the coronal magnetic field lines in the AR 13 076 were extrapolated with the Potential Field Source Surface (PFSS; Schrijver & De Rosa 2003) package of SolarSoftWare. The emission properties of the flare are investigated with the differential emission measure (DEM) method. The DEM method employs the *xrt\_dem\_iterative2.pro* in the SolarSoftWare package (Cheng et al. 2012; Song et al. 2014), and the EM maps at different temperature ranges are obtained by a set of AIA images in six channels (i.e., 94, 131, 171, 193, 211, and 335 Å).

In order to reconstruct the 3D magnetic configuration above the source region, the nonlinear-force-free-field (NLFFF) method was employed based on the photospheric vector magnetic fields observed by SDO/HMI. The HMI vector magnetograms were first removed the 180° ambiguity of the transverse components and then corrected the projection effect toward suitable boundary conditions for a force-free modeling. The calculations were performed within a box 161 × 121 × 121 uniformly distributed grid points with  $\Delta x = \Delta y = \Delta z = 2''$  (Guo et al. 2017). Furthermore, the twist number  $T_w$  of the extrapolated 3D magnetic fields were calculated through the method developed by Liu et al. (2016).

## 3. Results

The overview of AR 13 076 and the source region is shown in Figure 1. AR 13 076 consisted mainly of a positive sunspot (P1) surrounded by nearly stationary negative polarities (panel (b)). These formed a diffused moat region around P1. According to AIA 171 Å and the PFSS model, AR 13 076 was filled with clusters of magnetic loops and closed magnetic field lines (panel (c)). The source region was located at the southwest part of AR 13 076 (cyan box in panel (b)). It involved the main sunspot (P1), the trailing positive polarity (P2), as well as the surrounding negative polarities (N2-N3). In addition, an L-shaped filament existed in the source region. The profile of this filament was superimposed on HMI magnetogram maps that are rooted on P1 and N1, and the middle part of this filament passed through P2 and N2-N3.

Before the flare, an MFR was formed through tether-cutting reconnection between two sheared arches (L1 and L2). The overview of two sheared arches was present in the first row of Figure 2. L1 and L2 are separately located at the northern and southern sides of the source region that sheared passed through each other. The selected profiles of L1 and L2 were superposed on HMI magnetogram maps. L1 rooted on the P1 and N2-N3, and L2 rooted on the P2 and N1. Furthermore, the magnetic field evolution of two adjacent ends of L1 and L2 (P2 and N2-N3) were shown in the second and third rows. Initially, P2 and N2-N3 were left separately around 11:59:52 UT on 2022 August 11 (panel (d)), and then P2 and N2 converged toward each other. They contacted around 20:20:37 UT on 2022 August 11 (panel (e)). In the subsequent time, N2 also moved toward P2 (panels

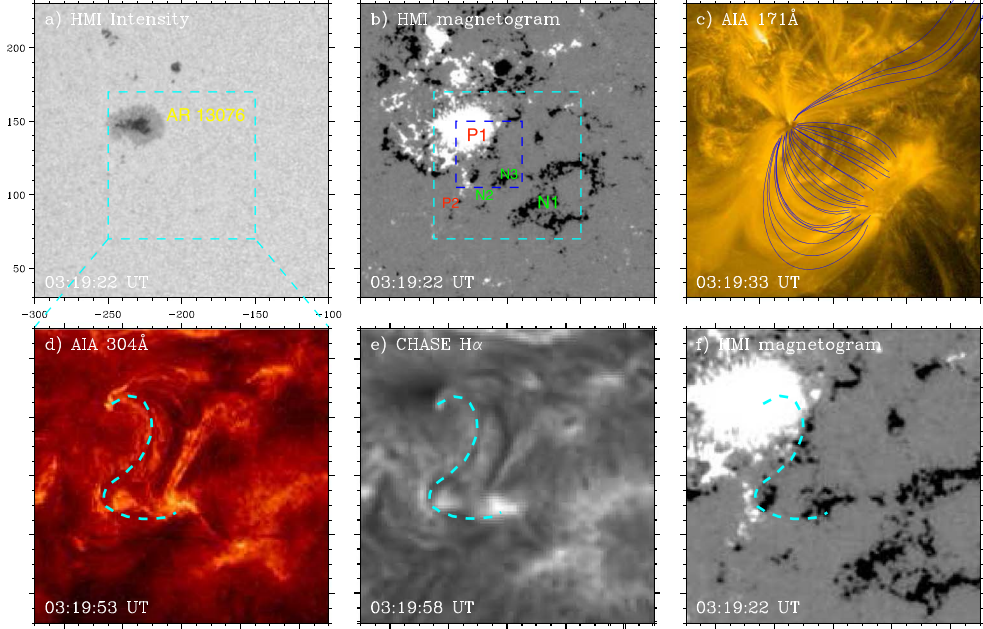


**Figure 1.** Overview of AR 13 076 and the source region. The first row shows AR 13 076 in HMI intensity maps (a), HMI magnetogram maps (b) and AIA 171 Å (c). The blue lines are extrapolated magnetic field lines in the PFSS model. The cyan box indicates the FOV of the source region. The blue box indicates the FOV of Figure 5. The second row shows the source region in AIA 304 Å (d), CHASE/H $\alpha$  (e), and HMI magnetogram maps (f). The cyan dashed line represents the profile of the filament.

(e)-(f)). To analyze the convergence motion of P2 and N2-N3, a horizontal slice was employed that extended from the eastern side of P2 and passed through P2 and N2-N3 (the yellow line). The time-distance plot was shown in panel (g). P2, N2 and N3 converged with the speeds of  $\sim 0.71 \text{ km s}^{-1}$ ,  $0.45 \text{ km s}^{-1}$ , and  $1.01 \text{ km s}^{-1}$ . Simultaneously, P2 canceled with N2-N3. The panels (e) and (f) showed that P2 evolved from a compact shape to a striped shape, and both N2-N3 shrunk. Note that the southern part of P2 at 06:30:37 UT on 2022 August 12 was considered since the northern part likely originated from other polarities from sunspot. Besides, the magnetic flux for the P2 and N2-N3 was measured (green box in panel (d)). After  $\sim 19:00$  UT on 2022 August 11, both the positive and negative flux experienced a remarkable decrease. The positive flux decreased  $\sim 3.3 \times 10^{20} \text{ Mx}$  and the negative flux decreased  $\sim 1.7 \times 10^{20} \text{ Mx}$ . Therefore, the adjacent ends of L1 and L2 experienced magnetic convergence and magnetic cancellation in the photosphere.

Accompanying with magnetic convergence and cancellation, MFR was formed through tether-cutting reconnection and the formation process was present in Figure 3. In three examples, the brightenings first appeared along L1 (green arrows) and then flux rope was formed (red arrows) that connected with the northern end of L1 and the western end of L2. The first example was particular that occurred a jet (blue arrow) simultaneously with the brightenings. The jet ejected from

the southern end of L1 to the eastern end of L2 that traced a small C-shaped loop. The small C-shaped loop was likely the production of the tether-cutting reconnection. The brightenings, the jet and the formed MFR, together with the magnetic convergence and cancellation of the adjacent ends of L1 and L2, are consistent with the physics picture of tether-cutting reconnection. Therefore, the MFR was likely formed by tether-cutting reconnection.

Furthermore, the formation of the MFR was checked by the NLFFF method at 00:00:00 UT and 04:00:00 UT on 2022 August 12 (Figure 4). The extrapolated magnetic field lines (pink) at 00:00 UT rooted on the P1 and N1 and the middle part passed through P2 and N2-N3, consisting with the magnetic configuration of the formed MFR (panel (a)). Then, the average twist number ( $\overline{T_w}$ ) for the region of southern footpoints of the extrapolated magnetic field lines (pink) in the photosphere was calculated (white dashed box). They were  $\overline{T_w} = 0.83$  at 00:00 UT and  $\overline{T_w} = 1.17$  at 04:00 UT. The increase of  $\overline{T_w}$  over time was consistent with the formation processes of an MFR. In addition, the twist number exceeded one turn at 04:00 UT that indicates it had been an MFR before eruption.

Then the magnetic field was rechecked and enlarged to the source region. In the source region, there existed continuous MMFs. The MMFs and their cancellation with the source region's PIL is shown in Figure 5. In two examples (first and second rows), the MMFs are type I MMFs that emerged in

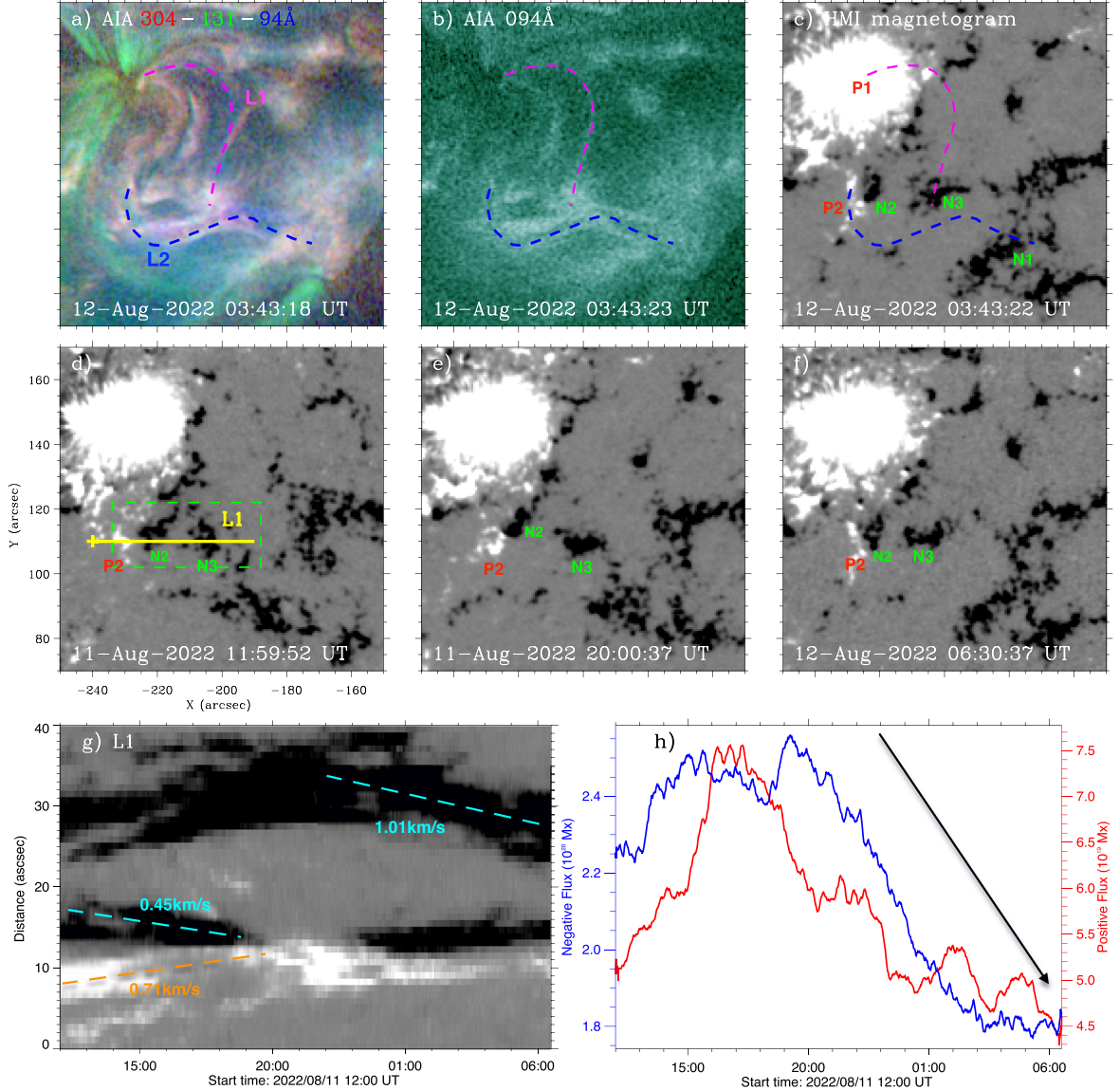


**Figure 2.** The magnetic convergence and cancellation of adjacent ends of two sheared arches (P2 and N2-N3) in the photosphere. The first row shows overview of two sheared arches (L1 and L2) in composite images, AIA 94 Å and HMI magnetogram maps. The purple and blue lines indicate the selected profiles of L1 and L2. The second row shows the magnetic convergence and cancellation of P2 and N2-N3. The time-distance plot is present in panel (g) along the yellow line in panel (d). The magnetic flux evolution for the green box in panel (d) was present in the panel (h). The black arrow indicates the downward trend of the positive and negative flux. An animation of the HMI magnetogram maps is available. The animated sequence runs from 12:00 UT on 11 August to 06:30 UT on August 12 and its real-time duration is 1 minute and 1 s.

(An animation of this figure is available.)

couple (blue arrows). Since the sunspot is positive, the emerging negative part of the MMFs were more obvious. The magnetic flux around the boundary of the sunspot (red box) was measured and focused mainly on the negative flux. It can be seen that the negative flux was nearly raised from zero, and simultaneously the positive flux also showed an overall increased trend (panel (g)). Therefore, it is confirmed that the MMFs emerged from the sunspot. After emergence, the MMFs moved toward the boundary of the moat region and

naturally converged to the source region's PIL. During the movement, the MMFs canceled with both the polarities of PIL (green arrows in the first example) and the footpoint of MFR (cyan arrows in the second example). Note that the magnetic flux cancellation caused by MMFs was continuous since they continuously emerged from the sunspot (the associated animation). Furthermore, the magnetic flux for the FOV of Figure 5 was measured and present in panel (h). It is shown that the positive magnetic flux experienced an abrupt decrease at the

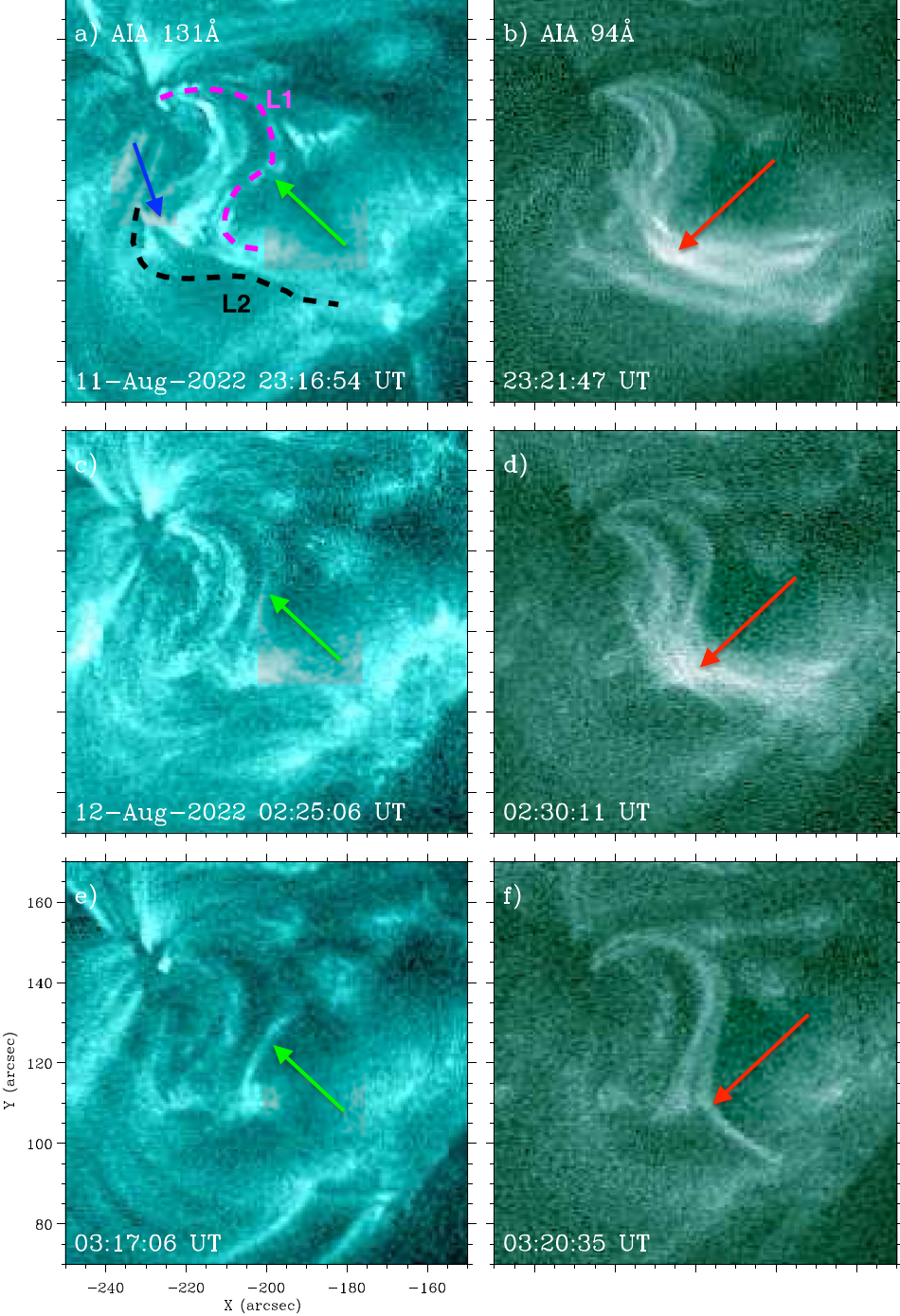


**Figure 3.** The formation of MFR through tether-cutting reconnection between L1 and L2 in AIA 131 and 94 Å. The three rows show three examples. The purple and cyan dashed lines represent two sheared arches facing each other. The green arrows represent the brightenings along L1. The red arrows represent the formed MFR. The blue arrow points to a jet that traced a small C-shaped loop. An animation of the AIA 131 and 94 Å maps is available. The animated sequence runs from 23:00 August 11 to 04:20 UT on August 12 and its real-time duration is 13 s.

(An animation of this figure is available.)

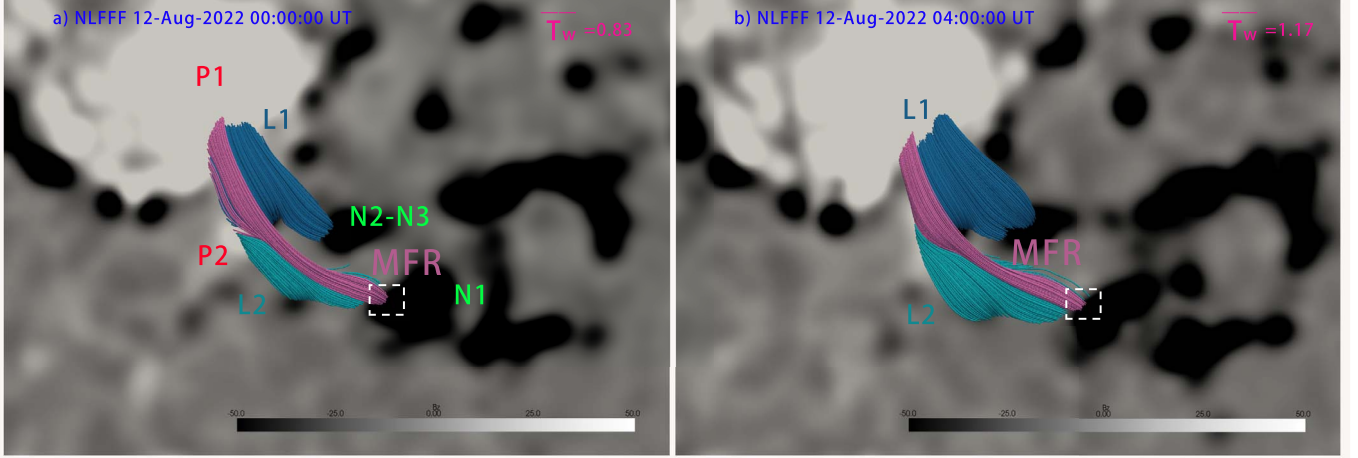


**Figure 4.** The formation of the MFR checked by extrapolated magnetic field lines from NLFFF method at 00:00:00 UT and 04:00:00 UT on 2022 August 12. The pink magnetic field lines indicate the formed MFR. The blue magnetic field lines indicate L1. The cyan magnetic field lines indicate L2. The calculated average twist number ( $\overline{T_w}$ ) of the plotted magnetic field lines (pink) in the photosphere was present in the Upper right corner of each panel. The background magnetic field is between  $-50$  and  $50$  Gauss.

onset of the eruption (black vertical line). The negative flux experienced bumps that indicates magnetic flux emergence and cancellation.

The formed MFR was likely destabilized by the magnetic flux cancellation that was intimately associated with the MMFs and started to erupt at around 04:53 UT (Figure 6). Two attractive flare ribbons (white arrows) and post-flare loops (yellow arrow in panel (e)) first appeared in the source region at the onset of the MFR eruption. The flare ribbons shared a nearly perpendicular configuration. The post-flare loops were weak and faded quickly. At this time, the erupted MFR was weak but became obvious at high latitude at around 04:57 UT (red arrows in panels (e) and (f)). During this phase, the erupted MFR rose slightly and stopped at a height (see associated animation). The eruption of the MFR was confined and eventually faded away.

The eruption of the MFR likely influenced the underlying filament. It erupted soon after the northern ribbons appeared under it (blue arrows in panel (a) of Figure 6). The filament showed overall western eruption and was accompanied by untwist motion (purple arrows in the first column of Figure 7 and associated animation). The ribbons transformed to the locations around two ends of the filament (white arrows in the second column). Obviously, the erupted filament was confined by its overlying magnetic loops (L1; orange arrows). Hence, the filament eruption was also confined.

The EM maps also clearly reveal two eruptions at three different temperature range of  $0.3\text{--}1.0$  MK (low),  $1.0\text{--}10$  MK (middle), and  $10.0\text{--}25.0$  MK (high) (Figure 8). In the first eruption, the flare ribbons were evident at all three temperature ranges (white arrows in the first column), the post-flare loops were visible at the middle temperature range (yellow arrow), and the erupted MFR mainly appeared at the high temperature

range (red arrows). In the second eruption, the erupted filament material was unambiguous at the low temperature range (purple arrows in the second column). It can be seen the erupted filament was confined by overlying loops that appeared at the middle temperature range (orange arrow). In addition, the emission at two ends of the filament was strong (white arrow in panel (b)), which consist with the location of the ribbons in filament eruption.

The successive eruptions of the MFR and the filament were captured by the GOES satellite (Figure 9). The SXR flux and its derivative profile clearly revealed two distinct peaks. The first peak occurred at  $\sim 04:58$  UT while the second peak occurred at  $\sim 05:10$  UT. It is consistent with the two-peak feature in intensity flux for the source region in AIA 1600, 304, and  $131\text{\AA}$ . In addition, the contours of flare ribbons were superposed on the magnetogram maps. As described in Zhu et al. (2018), Kazachenko et al. (2017), the reconnected flux can roughly estimated as the magnetic flux that was swept by flare ribbons at a given time. Both the reconnection flux and reconnection rate was calculated and present in panels (f) and (g). They also showed similar two-peaked features as those in SXR, its derivative and the intensity profiles for the source region. Hence, it is confirmed the confined two-peaked flare was induced by the successive eruptions of the MFR and the filament. Besides, both two flares lasted for about  $\sim 6$  minutes each. While the first peak in SXR's derivative profile was much stronger than the second peak.

#### 4. Conclusions and Discussion

Combing with high resolution observations from EAST, and SDO, we report a confined two-peaked flare induced by successive eruptions of an MFR and a filament. Before

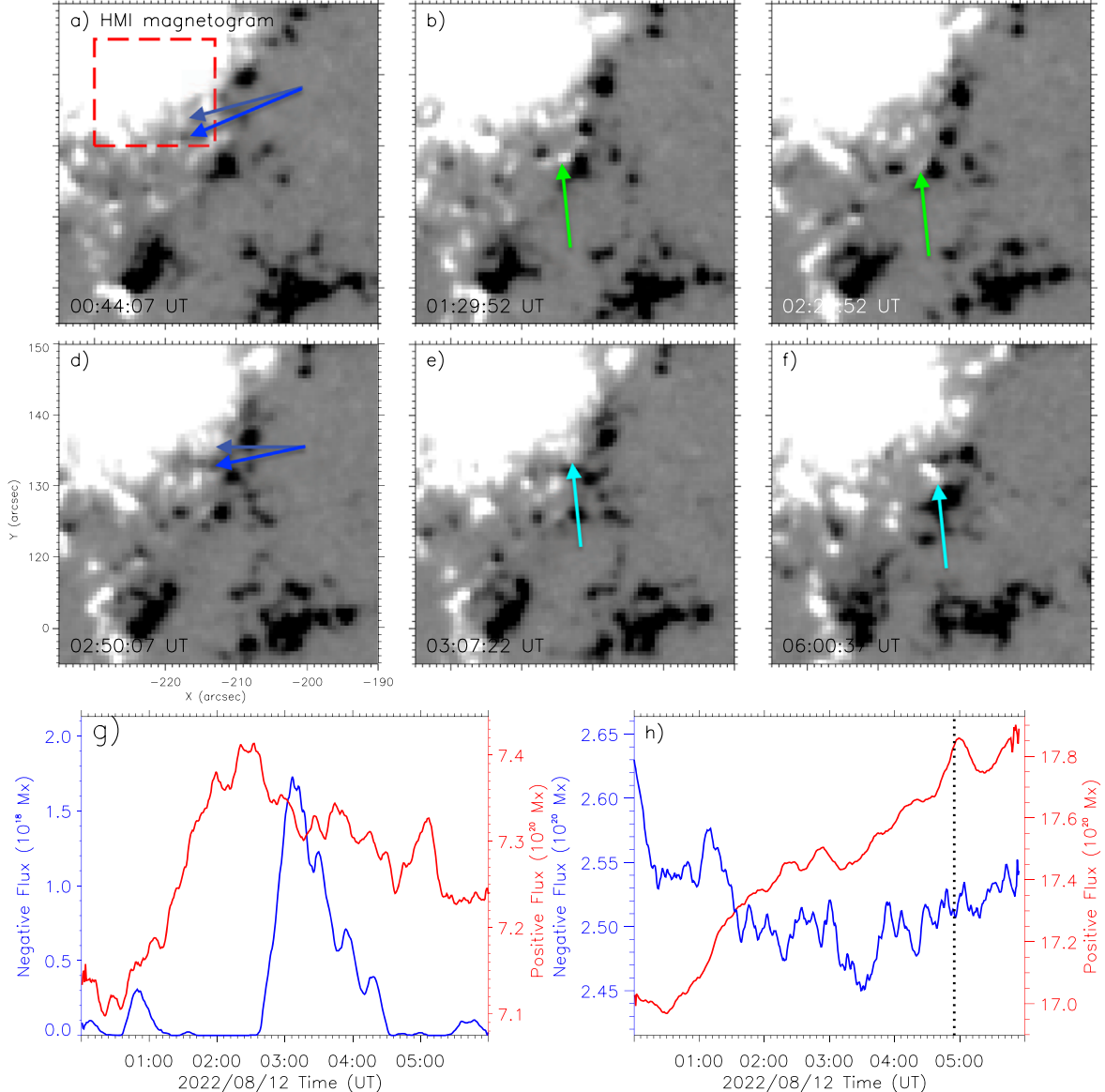


**Figure 5.** The MMFs and its cancellation with the source region’s PIL as well as footpoint of the MFR. The first and second rows show two examples. The blue arrows point to the MMFs in couple. The green and cyan arrows point to the canceled polarities of PIL. The magnetic flux for the red dashed box (g) and for this region (h). The vertical dashed line represents the onset of the eruption. An animation of the HMI magnetogram maps is available. Please see the associated animation in Figure 2.

(An animation of this figure is available.)

eruptions, the existed continuous MMFs in the source region and the MFR was formed through tether-cutting reconnection between two sheared arches (L1 and L2). The flare occurred after the MFR eruption that was confined by the overlying strong field. Interestingly, a small underlying filament immediately erupted, which was possibly destabilized by the flare ribbon. The successive eruptions were confirmed by the analysis of the emission measure and the reconnection fluxes. It is consistent with the two-peaked flare recorded by GOES XSR and its derivative profiles.

The MFR was likely formed by tether-cutting reconnection between two sheared arches (L1 and L2). Direct observations of tether-cutting reconnection are rare (Chen et al. 2014, 2018). In this case, L1 and L2 were sheared past each other, which was a good configuration for the occurrence of tether-cutting reconnection. The tether-cutting reconnection was likely driven by the convergence motion of two adjacent ends of two sheared arches in the photosphere. As the production of tether-cutting reconnection, the small C-shaped loop traced by the jet, the flux rope and the brightenings almost formed simultaneously. The

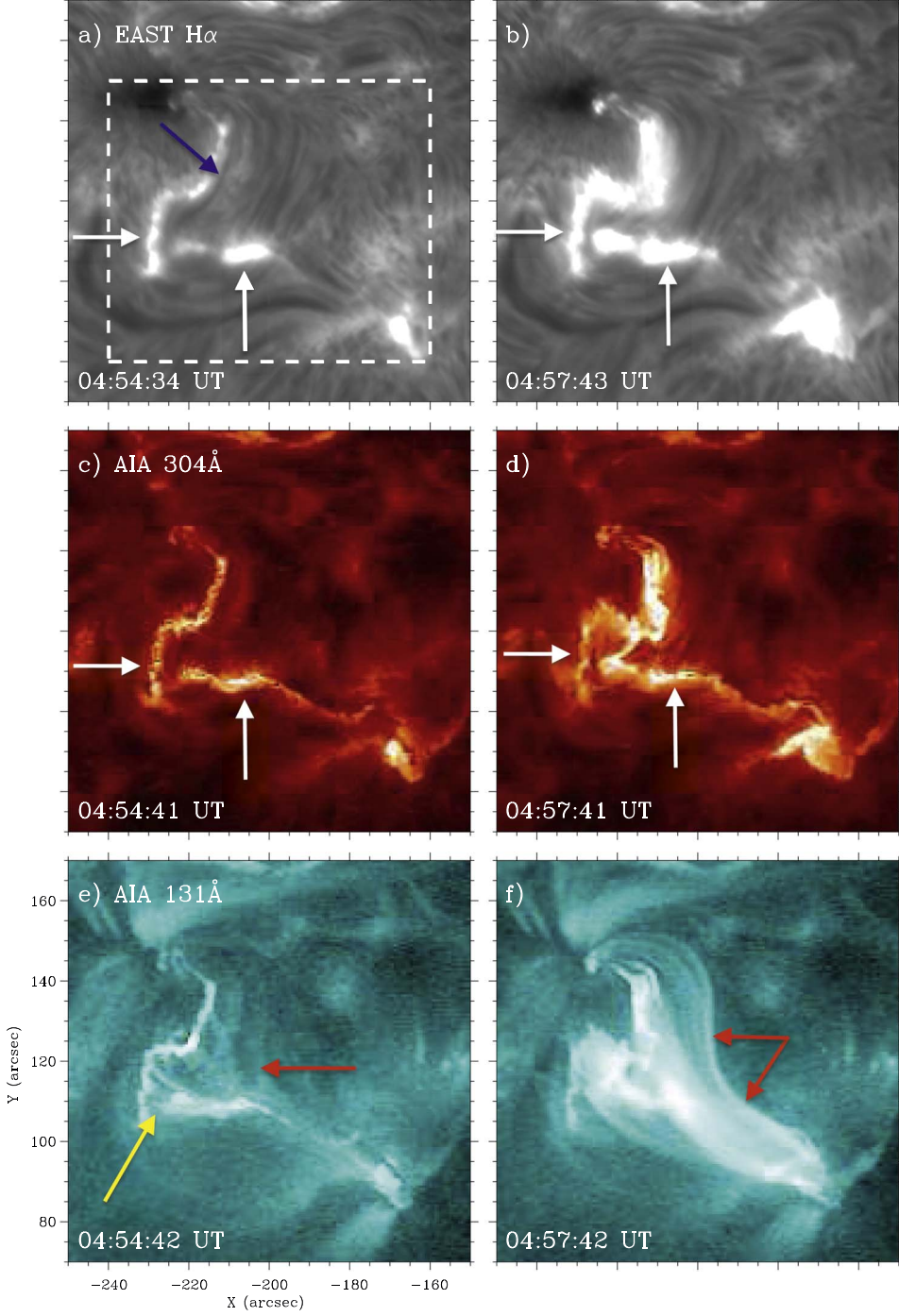


**Figure 6.** The eruption of the formed MFR in EAST H $\alpha$ , AIA 304 and 131  $\text{\AA}$ . Two columns show two moments during the MFR eruption. The white arrows indicate flare ribbons. The yellow arrow indicates post-flare loops. The red arrows indicate erupted MFR. The blue arrow indicates the ribbon appeared under the filament. An animation of the EAST, AIA 304, 131, 94  $\text{\AA}$  maps is available. The animated sequence runs from 04:50 to 05:20 UT on August 12 and its real-time duration is 6 s. (An animation of this figure is available.)

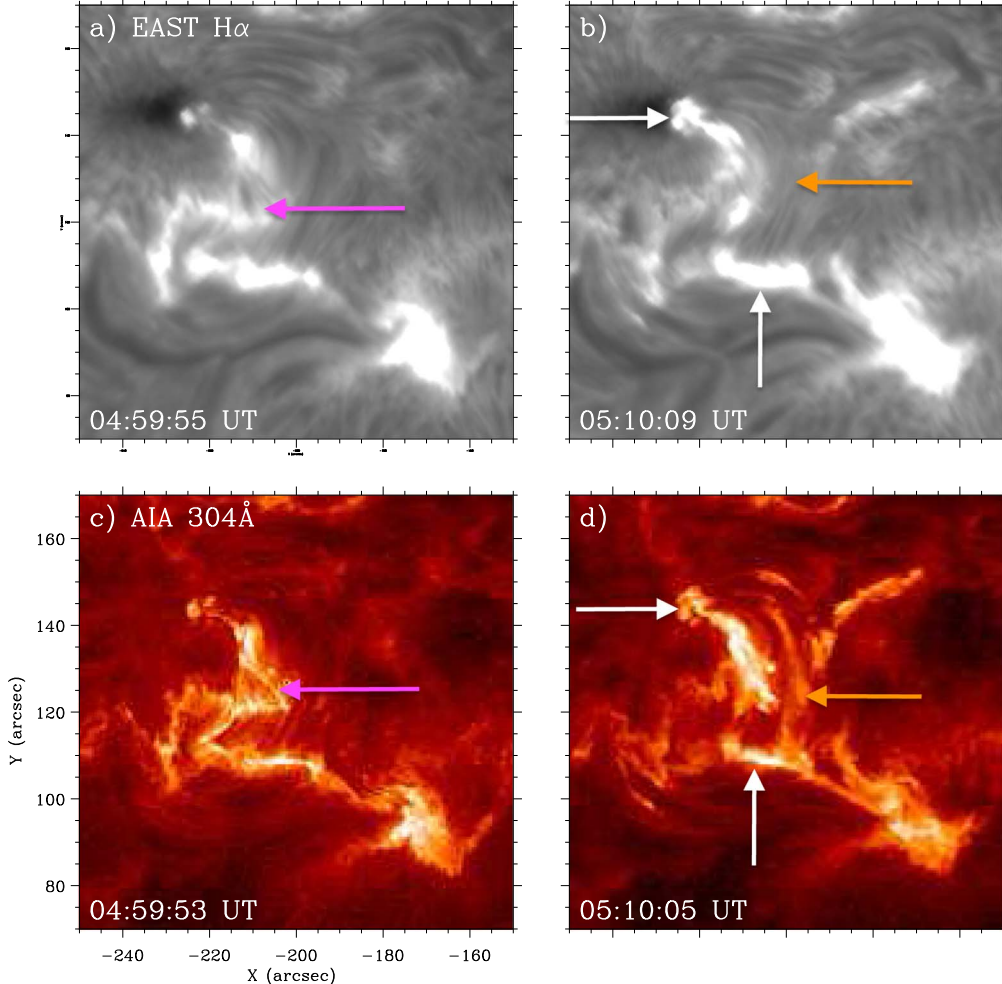


**Figure 7.** The filament eruption in EAST H $\alpha$  and AIA 304 Å. Two columns show two moments during the filament eruption. The purple arrows indicate the erupted filament. The orange arrows indicate overlying loops L1. The white arrows indicate new ribbons.

(An animation of this figure is available.)

magnetic cancellation of two adjacent ends in the photosphere was also observed accompanied with the tether-cutting reconnection. Based on these observations, it can be inferred there occurred tether-cutting reconnection between two sheared arches to form the MFR. In addition, L1 and L2 likely involved partial tether-cutting reconnection. Because the tether-cutting reconnection was relatively weak and L1 still confined erupted filament after MFR erupted. The partial tether-cutting reconnection is similar to Zheng et al. (2019).

The abrupt decrease of the positive magnetic flux has an intimate relationship with the onset of the eruption, which likely indicate the eruption was triggered by magnetic flux cancellation. The magnetic flux cancellation was accompanied by continuous MMFs. As being present in Figure 5, the cancellation site associated with MMFs mainly occurred at the footpoint of the MFR and the source region's PIL. On the one

hand, the magnetic flux emergence or cancellation around the footpoint of the MFR can influence its stability (Chen & Shibata 2000; Lin et al. 2001). On the other hand, the cancellation of the PIL can accumulate energy and flux for the overlying MFR (van Ballegooijen & Martens 1989). When the accumulated energy for an outward eruption of the MFR exceeds the energy of the restraining magnetic field, the MFR becomes unstable (Amari et al. 2010; Chen 2011; Sterling et al. 2011). However, it cannot rule out the cancellation which was caused by other magnetic polarities in the source region. But we hold the MMFs played an important role in the trigger of the eruption since the continuous MMFs flow brought sustained magnetic cancellation at the PIL as well as the footpoint of the MFR.

The confined two-peaked flare indicates two episodes of magnetic reconnection during the successive eruptions of the

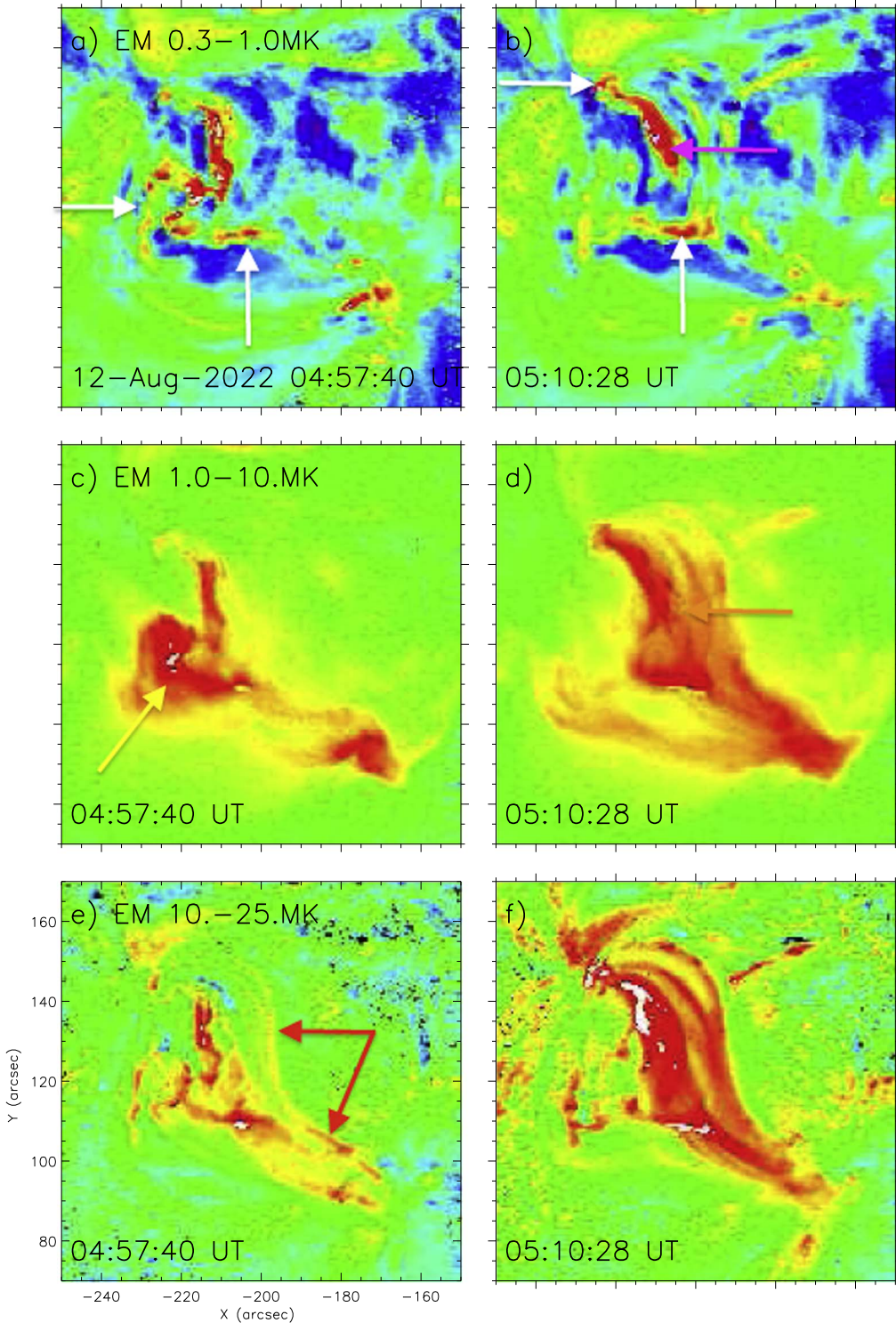


**Figure 8.** Two eruptions in EM maps at 0.3–1.0 MK (first row), 1.0–10.0 MK (second row), and 10.0–25.0 MK (third row). The white arrows indicate the ribbons in two eruption. The yellow arrow indicates the post-flare loops in the first eruption. The red arrows indicate the erupted MFR in the first eruption. The orange arrow indicates the overlying loops that confine the filament eruption. An animation of the EM maps at three temperature ranges is available. The animated sequence runs from 04:50 to 05:20 UT on August 12 and its real-time duration is 6 s.

(An animation of this figure is available.)

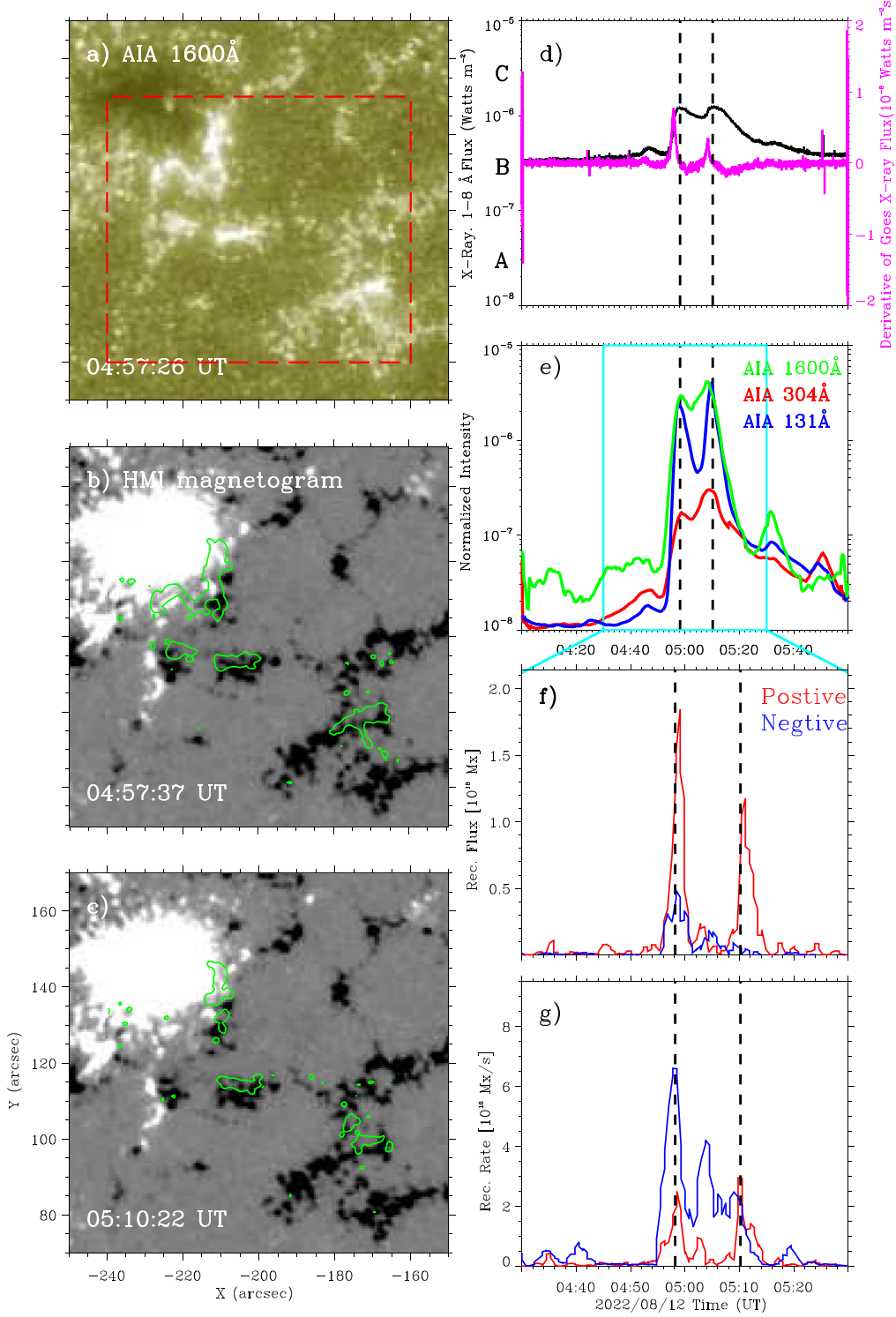


**Figure 9.** The flare ribbons in AIA 1600 Å and their contours superpose on the HMI magnetograms (first column). The GOES SXR flux and its derivative observed (d). The intensity curves in AIA 1600, 304, and 131 Å for the source region in panel (a) (e). The profiles of the reconnected flux and the reconnection rate for the positive (red) and negative (blue) magnetic flux ((f) and (g)). Two vertical dashed lines represent the two peak times of the flare.

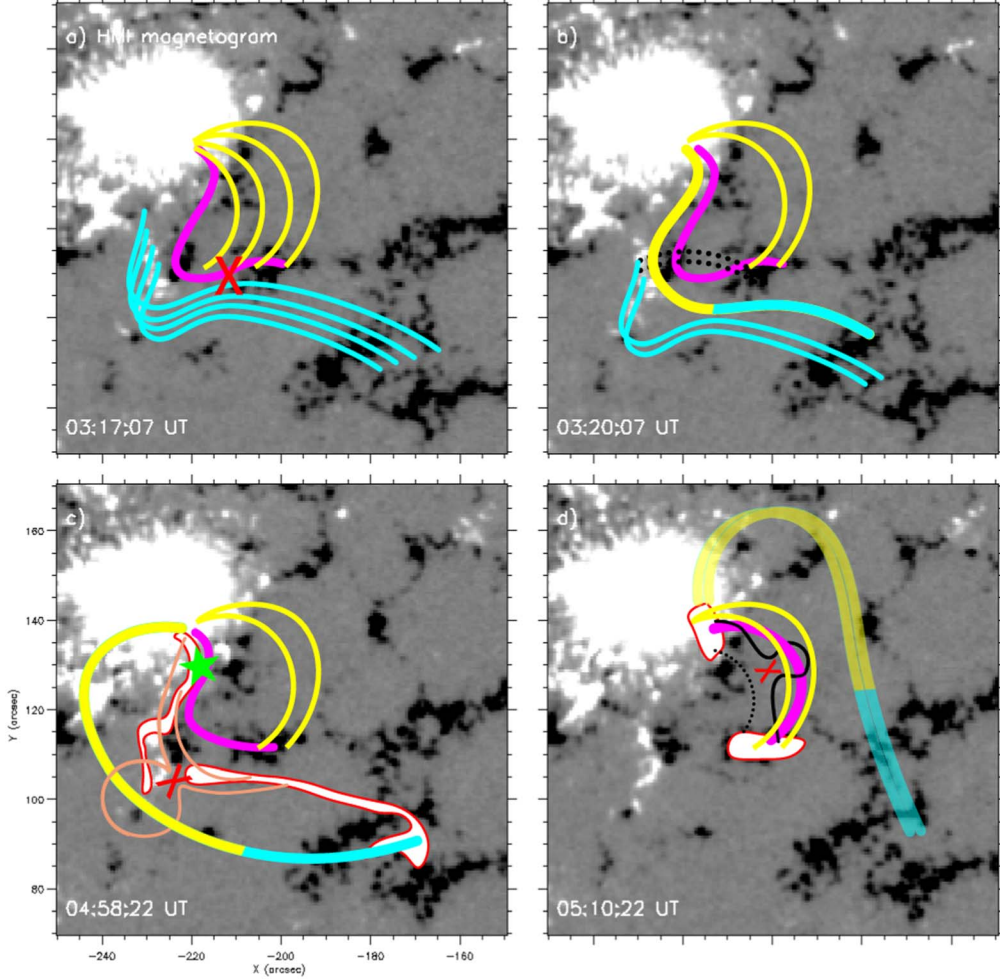


**Figure 10.** The scenario of the confined two-peaked flare. The formation of the MFR (first row). The yellow and cyan lines represent two sheared arches. The purple lines represent the filament underling L1. The “X” symbol indicates the occurrence of magnetic reconnection. The yellow-cyan line in panel (b) represents the formed MFR. The black dotted lines represent the post-reconnection loops in tether-cutting reconnection. The successive eruptions of the MFR and the filament (second row). The yellow-cyan line in panel (c) represents the raising MFR. The upper orange line represents the stretching magnetic field line. The lower orange line represents post-flare loops. The white patches with red contour represent flare ribbons. The weak yellow-cyan line in panel (d) represents the confined MFR which expanded and gradually fade away. The green asterisk in the panel (c) represents the ribbons influenced the filament. The upper black line in panel (d) represents the stretched magnetic field lines. The lower dotted line represents the likely post-flare loops.

MFR and the underlying filament. The first episode was likely caused by the eruption of the formed MFR. While the formed MFR was not erupted immediately after formation like Liu et al. (2010) and Joshi et al. (2015), but disappeared in AIA 131 and 94 Å. It is unclear the formed MFRs were really disappeared or simply due to the temperature decrease. A related event showed that the formed MFR could disappear in AIA channels but still exist in the source region, as evidenced by a filament formation through coronal condensation (see Figure 3 and the associated animation in Li et al. 2021). Moreover, the NLFFF method was employed and presented in Figure 4. It confirmed that an MFR existed before eruption. In addition, the twist number of the MFR exceeded one turn but

was still less twisted, which likely made it stable after formation. As for the second eruption, it was confined as the MFR eruption. Although both eruptions were confined, the MFR likely erupted more fully than the filament. Actually, the MFR erupted accompanied by obvious post-flare loops and two attractive flare ribbons. As for the filament eruption, it only accompanied by two compact ribbons around two ends. The SXR’s derivative profile also reveals that the first peak was much stronger than the second peak, which possibly means that the nonthermal emissions in the MFR eruption were more intense than those in the filament eruption.

Based on the above results and discussions, a scenario was proposed to interpret the confined two-peaked flare (Figure 10).

In the source region, there existed two sheared arches (L1 and L2; yellow and cyan lines in panel (a)) that separately were in the northern and southern sides. A filament was underlying L1 (purple line). Before eruption, L1 and L2 partially involved in the tether-cutting reconnection (“X” symbol in panel (a)). As a result, a MFR was formed (yellow-cyan line in panel (b)) with formation of lower post-reconnection loops (black dotted lines). The formed MFR likely destabilized by the magnetic flux cancellation that intimately associated with continuous MMFs in the source region and raised upward (panel (c)). The raising MFR stretched overlying loops above it, which made the anti-parallel magnetic field lines approach to each other (upper orange line), and magnetic reconnection occurred (“X” symbol). As the production of magnetic reconnection, the post-flare loops appeared at low latitude (lower orange line) and flare ribbons extended (white patch with red contour). The raising MFR eventually stopped at a height and gradually fade away (yellow-cyan line in panel (d)). Interestingly, the underlying filament was likely destabilized by ribbons that produced in MFR eruptions (green asterisk in the panel (c)). It erupted soon after the ribbons appeared under it. The erupted filament likely stretched the overlying loops (upper black lines) and produced lower post-reconnection loops (lower black dotted lines) through magnetic reconnection. Ribbons transformed to the location of filament’s two ends (white path with red contour in panel (d)). Eventually, the filament was also confined by overlying loops (L1; yellow lines).

In summary, this article reported a case study of the confined two-peaked flare and analyzed the associated eruptions. We suggest the confined two-peaked flare was caused by two distinct episodes of magnetic reconnection that took place during successive eruptions of the MFR and the underlying filament. However, more observations and simulations of two-peaked solar flares are required to improve our understanding of the complex evolution of the solar eruptions.

### Acknowledgments

The authors thank the EAST and SDO teams for the high-quality data. This work is supported by grants of the National

Natural Foundation of China (NSFC 12 073 016) and the open topic of the Yunnan Key Laboratory of Solar Physics and Space Science (YNSPCC202217).

### References

- Amari, T., Aly, J.-J., Mikic, Z., et al. 2010, *ApJL*, **717**, L26
- Antiochos, S. K., DeVore, C. R., & Klimchuk, J. A. 1999, *ApJ*, **510**, 485
- Chen, H., Duan, Y., Yang, J., et al. 2018, *ApJ*, **869**, 78
- Chen, H., Zhang, J., Cheng, X., et al. 2014, *ApJL*, **797**, L15
- Chen, P. F. 2011, *LRSP*, **8**, 1
- Chen, P. F., & Shibata, K. 2000, *ApJ*, **545**, 524
- Cheng, X., Zhang, J., Saar, S. H., et al. 2012, *ApJ*, **761**, 62
- Fan, Y. 2005, *ApJ*, **630**, 543
- Forbes, T. G. 2000, *JGR*, **105**, 23153
- Guo, Y., Cheng, X., & Ding, M. 2017, *ScChD*, **60**, 1408
- Harvey, K., & Harvey, J. 1973, *SoPh*, **28**, 61
- Ji, H., Wang, H., Schmahl, E. J., et al. 2003, *ApJL*, **595**, L135
- Joshi, N. C., Liu, C., Sun, X., et al. 2015, *ApJ*, **812**, 50
- Joshi, R., Mandrini, C. H., Chandra, R., et al. 2022, *SoPh*, **297**, 81
- Kazachenko, M. D., Lynch, B. J., Welsch, B. T., et al. 2017, *ApJ*, **845**, 49
- Kliem, B., & Török, T. 2006, *PhRvL*, **96**, 255002
- Lemen, J. R., Title, A. M., Akin, D. J., et al. 2012, *SoPh*, **275**, 17
- Li, C., Fang, C., Li, Z., et al. 2022, *SCPMA*, **65**, 289602
- Li, L., Peter, H., Chitta, L. P., et al. 2021, *ApJL*, **919**, L21
- Lin, J., Forbes, T. G., & Isenberg, P. A. 2001, *JGR*, **106**, 25053
- Liu, R. 2020, *RAA*, **20**, 165
- Liu, R., Kliem, B., Titov, V. S., et al. 2016, *ApJ*, **818**, 148
- Liu, R., Liu, C., Wang, S., et al. 2010, *ApJL*, **725**, L84
- Low, B. C. 2001, *JGR*, **106**, 25141
- Mackay, D. H., Karpen, J. T., Ballester, J. L., et al. 2010, *SSRv*, **151**, 333
- Martin, S. F. 1998, *SoPh*, **182**, 107
- Moore, R. L., Sterling, A. C., Hudson, H. S., et al. 2001, *ApJ*, **552**, 833
- Ning, H., Chen, Y., Wu, Z., et al. 2018, *ApJ*, **854**, 178
- Paraschiv, A. R., Donea, A., & Leka, K. D. 2020, *ApJ*, **891**, 149
- Patsourakos, S., Vourlidas, A., Török, T., et al. 2020, *SSRv*, **216**, 131
- Pesnell, W. D., Thompson, B. J., & Chamberlin, P. C. 2012, *SoPh*, **275**, 3
- Rao, C., Rao, X., Du, Z., et al. 2022, *RAA*, **22**, 065003
- Scherrer, P. H., Schou, J., Bush, R. I., et al. 2012, *SoPh*, **275**, 207
- Schrijver, C. J., & De Rosa, M. L. 2003, *SoPh*, **212**, 165
- Song, H. Q., Zhang, J., Cheng, X., et al. 2014, *ApJ*, **784**, 48
- Sterling, A. C., Chifor, C., Mason, H. E., et al. 2010, *A&A*, **521**, A49
- Sterling, A. C., Moore, R. L., & Freeland, S. L. 2011, *ApJL*, **731**, L3
- Török, T., Kliem, B., & Titov, V. S. 2004, *A&A*, **413**, L27
- van Ballegooijen, A. A., & Martens, P. C. H. 1989, *ApJ*, **343**, 971
- Yang, S., Zhang, J., Song, Q., et al. 2019, *ApJ*, **878**, 38
- Zheng, R., Liu, Y., Zhang, L., et al. 2023, *ApJL*, **942**, L16
- Zheng, R., Yang, S., Rao, C., et al. 2019, *ApJ*, **875**, 71
- Zhu, C., Qiu, J., & Longcope, D. W. 2018, *ApJ*, **856**, 27